

Inertial-Range Suppression and Ponderomotive Density Cavitation in Broadband Sub-Alfvénic Turbulence under Plasma Sheet Boundary Layer Conditions

Mani K Chettri ^{*1}, Vivek Shrivastav ¹, Britan Singh ¹, Rupak Mukherjee ¹, and Hemam D. Singh ^{*2}

¹Department of Physics, Sikkim University, Gangtok 737102, Sikkim, India

²Department of Physics, Netaji Subhas University of Technology, New Delhi 110078, India

*Corresponding authors:

Mani K Chettri: mkchettri8@gmail.com

Hemam D. Singh: hemam.singh@nsut.ac.in

Abstract

Kinetic Alfvén waves (KAWs) are among the most pervasive electromagnetic fluctuations in magnetized astrophysical plasmas, from Earth’s magnetospheric boundary layers to the turbulent intracluster medium of galaxy clusters. Their ponderomotive coupling to compressive density fluctuations remains incompletely understood in the broadband turbulent regime. We present two-dimensional pseudospectral simulations of the modified nonlinear Schrödinger–magnetosonic (MNLS–MS) system governing KAW envelopes, initialized with a broadband power-law spectrum ($|\psi(\mathbf{k})|^2 \propto k^{-5/6}$) spanning many interacting modes, at $\beta \sim 0.1$ – 0.3 representative of plasma sheet boundary layer (PSBL) conditions. A fourth-order Runge–Kutta scheme on a 256×256 grid integrates the system to $t = 40$ (normalized), with total energy conserved to within 0.085%. The nonlinearity parameter $\chi_{\text{NL}} \approx 0.25$ confirms broadband sub-Alfvénic turbulence throughout. Magnetic field intensity and plasma density develop spatially intermittent, filamentary structures within the first few wave periods, consistent with ponderomotive density cavitation and plasma expulsion from wave-intense regions. The magnetic energy spectra show inertial-range suppression, with a rapid transition from injection ($k < 0.3$) to dissipation without an extended power-law cascade, in agreement with the moderate magnetic Reynolds number ($\text{Re} \sim 250$ – 370) of the simulation and the observationally constrained range for PSBL turbulence. These results provide numerical evidence that broadband KAW turbulence self-organizes into coherent density structures at kinetic scales, and that the spectral character of such turbulence is governed primarily by moderate-Reynolds-number constraints rather than by the wave physics alone.

Keywords: kinetic Alfvén waves; modified nonlinear Schrödinger equation; plasma turbulence; ponderomotive force; density cavities; pseudospectral method; plasma sheet boundary layer; astrophysical plasmas

1 Introduction

Alfvénic turbulence is a universal feature of magnetized astrophysical plasmas, mediating the transfer of energy from the large fluid scales at which it is injected down to the kinetic scales of individual particles, where it is ultimately thermalized. At perpendicular spatial scales approaching the ion gyroradius ρ_i or the ion inertial length d_i , ideal shear Alfvén waves acquire dispersive corrections and transform into kinetic Alfvén waves (KAWs), a transition that is observationally well established in the solar wind (Leamon et al., 1999; Bale et al., 2005; Chen et al., 2013; Sahraoui et al., 2009), in Earth’s magnetosphere (Chaston et al., 2008; Wygant et al., 2002), and in the magnetosheath (Roberts et al., 2018; Gershman et al., 2017b). KAWs carry a finite parallel electric field E_{\parallel} that opens a direct channel for wave-particle energy exchange through Landau damping (Howes et al., 2008; Chen et al., 2019), and at finite amplitude they exert a ponderomotive force on the bulk plasma, a low-frequency, gradient-driven pressure $\propto -\nabla|\delta B_y|^2/8\pi$, which expels ions from regions of high wave intensity and forms localized density depletions. These two effects, particle heating and density structuring, make KAWs important agents not only in Earth’s magnetotail (Wygant et al., 2002; Stawarz et al., 2017; Chettri et al., 2026) but also in the broader context of astrophysical plasma heating. In solar coronal loops, parametric decay of standing Alfvén waves generates compressive daughter modes with observationally testable signatures (Terradas et al., 2022). In the inner heliosphere, coupled KAW and ion-acoustic wave dynamics have been studied using Parker Solar Probe data (Chettri et al., 2024). In the interstellar medium, kinetic-scale Alfvénic turbulence shapes the scattering properties of pulsars and governs cosmic-ray transport (Lazarian and Beresnyak, 2006; Yan and Lazarian, 2004). In the turbulent intracluster medium of galaxy clusters, where magnetic fields thread hot, weakly collisional gas, analogous wave-plasma interactions on scales below the Coulomb mean free path have been invoked to explain observed magnetic field tangling and sub-Larmor density fluctuations (Brunetti and Lazarian, 2007; Schekochihin et al., 2009).

The theoretical framework for KAW nonlinear dynamics rests on foundational studies spanning several decades. Hasegawa and Chen (1976) identified parametric decay as the primary instability by which a monochromatic KAW transfers energy to compressive daughter modes. Shukla and Stenflo (1999) derived the coupled KAW–magnetosonic equations that describe ponderomotive density cavity formation in the quasi-static limit and demonstrated the linear anti-correlation $n/n_0 \propto -|\delta B_y|^2$. More recently, three-dimensional hybrid simulations of circularly polarized Alfvén waves by Verscharen et al. (2024) have confirmed that the parametric decay instability operates across a broad spectrum of wave vectors. Goldreich and Sridhar (1995) and Boldyrev and Perez (2012) established the theoretical spectral scalings expected when Alfvénic turbulence reaches a critically balanced cascade, providing benchmarks against which kinetic-scale simulations can be compared. Our group recently derived and validated a modified nonlinear Schrödinger equation (MNLSE) framework that self-consistently incorporates KAW dispersion, ponderomotive nonlinearity, and phenomenological Landau damping, and tested it against MMS magnetosheath observations (Chettri et al., 2025). Separately, Chettri et al. (2026) reported direct MMS observations of KAW turbulence signatures in the outer PSBL, establishing the observational context for the present numerical study. Nevertheless, the ponderomotive scaling relation has been tested chiefly in analytical or single-wave-packet settings; how it behaves within a broadband fluctuation environment where multiple interacting modes compete and interfere remains much less well characterized.

This gap motivates the present work. We solve the coupled MNLSE–magnetosonic system of Chettri et al. (2025) in two spatial dimensions using a pseudospectral method on

a 256×256 grid, initialized with a broadband turbulent spectrum representative of PSBL conditions. The PSBL provides a well-observed astrophysical boundary layer where magnetic energy, particle fluxes, and broadband electromagnetic turbulence coexist at directly measurable intensities, giving concrete observational anchors for the simulation parameters. Our goals are fourfold: (1) to examine how KAW ponderomotive coupling operates when the driving is turbulent rather than monochromatic; (2) to characterize the spatial structure and temporal persistence of the resulting density fluctuations; (3) to assess the spectral character of the magnetic energy cascade at moderate Reynolds numbers; and (4) to provide diagnostics (energy conservation, nonlinearity parameter, energy partition) that allow meaningful comparison with in-situ observations and theoretical expectations.

Section 2 presents the governing MNLS–MS equations and the ponderomotive scaling prediction. The numerical method, parameters, and initialization are described in Section 3. Results are presented in Section 4, followed by discussion in Section 5 and a summary in Section 6.

2 Theoretical Framework

We consider a magnetized plasma with a uniform ambient magnetic field $\mathbf{B}_0 = B_0 \hat{z}$ and background density n_0 . The total density is $N = n_0 + n$, with n the perturbation. The KAW magnetic field perturbation is written as a slowly-varying complex envelope, $\delta B_y = \text{Re}[\psi e^{i(k_0 x - \omega_0 t)}]$, where $\psi(x, z, t)$ evolves on timescales much longer than ω_0^{-1} . In the slowly-varying envelope approximation, the time-averaged magnetic field intensity is $\langle |\delta B_y|^2 \rangle = |\psi|^2/2$; we refer to $|\delta B_y|^2$ (as labelled in the figures) and $|\psi|^2$ interchangeably throughout, noting that they carry the same spatial and temporal structure.

2.1 Modified Nonlinear Schrödinger Equation

Following Chettri et al. (2025), the slowly-varying envelope ψ satisfies the modified nonlinear Schrödinger (MNLS) equation

$$i \frac{\partial \psi}{\partial t} + P \frac{\partial^2 \psi}{\partial x^2} + Q |\psi|^2 \psi + i\Gamma \psi = 0, \quad (1)$$

whose three coefficients encode the dispersive, ponderomotive, and dissipative physics of the KAW, respectively.

The *dispersion coefficient* P follows from the KAW dispersion relation $\omega^2 = k_z^2 v_A^2 (1 + k_\perp^2 \rho_s^2)$:

$$P = \frac{1}{2} \frac{\partial^2 \omega}{\partial k_\perp^2} = \frac{v_A^2 \rho_s^2 k_z^2}{2 \omega_0 (1 + k_0^2 \rho_s^2)}, \quad (2)$$

where $v_A = B_0 / \sqrt{4\pi n_0 m_i}$ is the Alfvén speed, $\rho_s = C_s / \Omega_i$ is the ion-sound gyroradius, $C_s = \sqrt{k_B T_e / m_i}$ is the ion-sound speed, and $\Omega_i = e B_0 / (m_i c)$ is the ion gyrofrequency. The ρ_s^2 factor makes dispersion a purely kinetic effect, absent in ideal MHD.

The *ponderomotive nonlinearity coefficient* Q arises from the self-consistent coupling between wave pressure $|\psi|^2 / 8\pi$ and the magnetosonic density response:

$$Q = \frac{\omega_0 \Gamma_2}{C_s^2}, \quad \Gamma_2 = \frac{v_A^2}{4 B_0^2}. \quad (3)$$

Because $Q > 0$, regions of enhanced $|\psi|^2$ expel plasma and decrease the local refractive index, reinforcing the growth of filamentary intensity peaks through ponderomotive self-focusing (Shukla and Stenflo, 1999; Hasegawa and Chen, 1976).

The *Landau damping coefficient* Γ approximates the collisionless electron (and ion) damping of the KAW envelope. Following [Chettri et al. \(2025\)](#), it is evaluated from the imaginary part of the linearized kinetic dispersion function at (k_0, ω_0) :

$$\Gamma = \frac{|\text{Im}[\omega_{\text{kin}}(k_0)]|}{\omega_0} \omega_0. \quad (4)$$

In the low- β PSBL regime ($\beta \sim 0.1\text{--}0.3$, $T_i/T_e = 2$), resonant damping is well below the wave frequency, so Γ acts as a perturbative correction to the dispersive and nonlinear dynamics. It is retained for consistency with the high- β magnetosheath analysis of [Chettri et al. \(2025\)](#); the full kinetic treatment of velocity-space resonances is deferred to gyrokinetic approaches such as those described in [Schekochihin et al. \(2009\)](#) and [Howes et al. \(2008\)](#).

2.2 Ponderomotively Driven Density Equation

The ponderomotive force $\mathbf{f}_{\text{pond}} \propto -\nabla|\psi|^2$ drives compressive fluctuations through the magnetosonic branch. Following [Shukla and Stenflo \(1999\)](#) and [Chettri et al. \(2025\)](#), the general form of the density equation is

$$\left(\frac{\partial^2}{\partial t^2} - C_s^2 \nabla^2 \right) \frac{n}{n_0} = \Gamma_2 \nabla^2 |\psi|^2. \quad (5)$$

In the strongly magnetized PSBL regime ($\beta \ll 1$), compressive perturbations propagate preferentially along the ambient field $\mathbf{B}_0 = B_0 \hat{z}$, and cross-field acoustic transport is suppressed by the strong magnetic pressure. The density response is therefore governed primarily by the field-aligned component of the ponderomotive gradient. We accordingly adopt the parallel-propagation approximation $\nabla^2 \rightarrow \partial^2/\partial z^2$, reducing the density equation to

$$\left(\frac{\partial^2}{\partial t^2} - C_s^2 \frac{\partial^2}{\partial z^2} \right) \frac{n}{n_0} = \Gamma_2 \frac{\partial^2}{\partial z^2} |\psi|^2, \quad (6)$$

with Γ_2 as defined in equation (3). This approximation is appropriate for the low- β conditions explored here, where the acoustic speed satisfies $C_s \ll v_A$ and the perpendicular pressure balance is maintained by the ambient magnetic field rather than by the thermal plasma pressure. Equations (1) and (6) form the coupled MNLS–MS system solved in the present simulations.

In the quasi-static limit ($|\partial^2/\partial t^2| \ll C_s^2 k_z^2$), the common parallel Laplacian cancels and equation (6) reduces to the ponderomotive scaling relation

$$\frac{n}{n_0} \approx -\frac{\Gamma_2}{C_s^2} |\psi|^2 = -\frac{v_A^2}{4B_0^2 C_s^2} |\psi|^2, \quad (7)$$

predicting a linear anti-correlation between local wave intensity and plasma density with slope $-\Gamma_2/C_s^2$.

The density perturbations generated by equation (6) represent quasi-modes continuously maintained by the KAW ponderomotive source, rather than freely propagating ion acoustic waves. In the magnetotail, where $T_i/T_e \sim 1\text{--}3$, ion Landau damping strongly suppresses free acoustic propagation ([Verscharen et al., 2024](#); [Terradas et al., 2022](#)). Energy transferred from the KAW envelope into these density quasi-modes can thermalize rapidly via ion Landau damping, providing a direct ion heating channel not resolved by the present fluid model but important for the astrophysical interpretation.

We note that the cubic nonlinearity $Q|\psi|^2\psi$ in equation (1) already embeds the quasi-static density response (equation 7) within the envelope evolution: the coefficient $Q = \omega_0\Gamma_2/C_s^2$ is precisely the ponderomotive coupling strength evaluated in the adiabatic limit. The dynamical density equation (6) is solved separately to resolve finite-frequency corrections to this adiabatic balance and to provide the spatially resolved density field for diagnostic comparison with spacecraft observations. Feedback of the dynamical density on the envelope beyond the quasi-static limit is a higher-order correction, small by $\mathcal{O}(\chi_{\text{NL}}^2)$ in the sub-Alfvénic regime explored here ($\chi_{\text{NL}} \approx 0.25$).

3 Numerical Method and Simulation Parameters

3.1 Algorithm

The MNLS–MS system, equations (1) and (6), is solved in two spatial dimensions (x, z) using a pseudospectral method following the approach of Chettri et al. (2025). All spatial derivatives are computed in Fourier space via the Fast Fourier Transform (FFT), which provides spectral accuracy for smooth fields. Time integration uses a classical fourth-order Runge–Kutta (RK4) scheme with time step $\Delta t = 10^{-5}$ (normalized).

At each time step, the complex envelope ψ and density field n/n_0 are transformed to wavenumber space. Spatial derivative operators are applied algebraically, and the 2/3-rule dealiasing mask is applied to suppress aliasing from the nonlinear terms $|\psi|^2\psi$ and $|\psi|^2$ before transforming back to physical space. The Landau damping term $\Gamma\psi$ is also evaluated spectrally. Grid-scale noise is controlled by a high-order hyperviscosity operator $-\nu_h k^6$ applied to wavenumbers above $3k_{\text{max}}/4$, with coefficient $\nu_h = 10^{-9}$ chosen to confine energy dissipation to the grid scale without contaminating physical-scale dynamics. The density equation (6) is cast as a first-order system by introducing the auxiliary variable $w = \partial(n/n_0)/\partial t$, and both n/n_0 and w are advanced together with the envelope by RK4. The parallel-derivative operator $\partial^2/\partial z^2$ in equation (6) is evaluated as $-k_z^2$ in Fourier space.

3.2 Simulation Parameters

Table 1 lists all simulation parameters. Plasma parameters are chosen to represent the near-Earth PSBL at $X_{\text{GSM}} \approx -7R_E$, based on observational compilations from Stawarz et al. (2017) and statistical analyses in Du et al. (2011) and Zhou et al. (2012). The values $B_0 = 63$ nT, $n_0 = 0.72$ cm $^{-3}$, and $T_e = 2.6$ keV are taken directly from observations, and the temperature ratio $T_i/T_e = 2$ is consistent with Hydra spacecraft measurements in this region (Shrivastava et al., 2015). Together these yield $\beta \sim 0.1$ – 0.3 , placing the simulation in the warm plasma regime where electromagnetic KAW generation and propagation are most efficient (Denton et al., 2010).

Spatial coordinates are normalized to the ion inertial length $d_i = c/\omega_{pi}$, time to Ω_i^{-1} , magnetic field to B_0 , and density to n_0 . In these normalized units, v_A and ρ_s are both set to unity for computational convenience; the physical plasma beta enters through the dimensionless coefficients P , Q , and Γ , which are computed from the PSBL parameters listed in Table 1.

3.3 Initialization

The simulation begins with a broadband turbulent spectrum, in deliberate contrast to single-wave-packet approaches. The initial complex envelope in Fourier space is assigned a power-

Table 1: Simulation parameters. Observed plasma values B_0 , n_0 , and T_e are from [Stawarz et al. \(2017\)](#); T_i/T_e from [Shrivastava et al. \(2015\)](#).

Parameter	Value
Grid resolution	256×256
Domain size	$L_x \times L_z = (2\pi/0.1)^2$
Time step Δt	10^{-5}
t_{\max}	40
Alfvén speed v_A	1.0
Ion-sound gyroradius ρ_s	1.0
Plasma beta β	0.1–0.3
Hyperviscosity ν_h	10^{-9}
B_0	63 nT
n_0	0.72 cm^{-3}
T_e	2.6 keV
T_i/T_e	2

law amplitude $|\psi(\mathbf{k})|^2 \propto (k/k_{\min})^{-5/6}$ over the injection range $k_{\min} = 0.08$ to $k_{\max} = 0.5$ (normalized), with random phases drawn uniformly from $[0, 2\pi)$ and a fixed seed for reproducibility. The real-space field is normalized to a standard deviation equal to the desired amplitude $A_B = 0.5$. The density is initialized with a correlated but phase-independent field at amplitude $0.4 A_B$, and the auxiliary velocity variable w is set from approximate acoustic balance. This procedure places turbulent energy across many modes from the outset, eliminating the artificial transient that arises when a single wave packet is allowed to self-organize under ponderomotive forcing.

4 Simulation Results

4.1 Energy Conservation and Nonlinearity

Figure 1 shows three global diagnostics tracked throughout the run. Panel (a) displays the total energy E_{tot} , the sum of magnetic (KAW), kinetic (wave), and acoustic (density) components integrated over the domain. Over the full integration to $t = 40$, the energy drifts by only -0.085% , monotonically and without runaway behaviour, confirming that the hyperviscosity removes energy at grid scales rather than allowing it to accumulate at physical ones.

Panel (b) shows the partition between magnetic and density energy on a logarithmic scale. The magnetic component dominates throughout at a roughly constant normalized value near 0.25; the acoustic component sits near 10^{-3} and declines slowly. This two-order-of-magnitude gap is physically meaningful: because energy transferred from KAWs to compressive modes scales as $(n/n_0)^2$, and the density response remains small at the explored amplitudes, the acoustic component necessarily carries a minor share of the total budget. This does not imply weak ponderomotive coupling; the density structures in Section 4.3 are spatially prominent. It reflects the dominance of the Alfvénic energy reservoir.

Panel (c) shows the nonlinearity parameter $\chi_{\text{NL}} = \sigma(|\delta B_y| |n/n_0|) / \sigma(|\delta B_y|)$, which measures the relative strength of the ponderomotive coupling term against the linear envelope amplitude. The values remain in the range 0.2–0.28 throughout, well below the critical threshold $\chi_{\text{NL}} = 1$ at which the transition to strong turbulence occurs. The simulation therefore operates in the sub-Alfvénic, moderately nonlinear regime characteristic of quieter PSBL intervals and of many other astrophysical boundary layers (Galtier et al., 2000; Matthaeus and Velli, 2011).

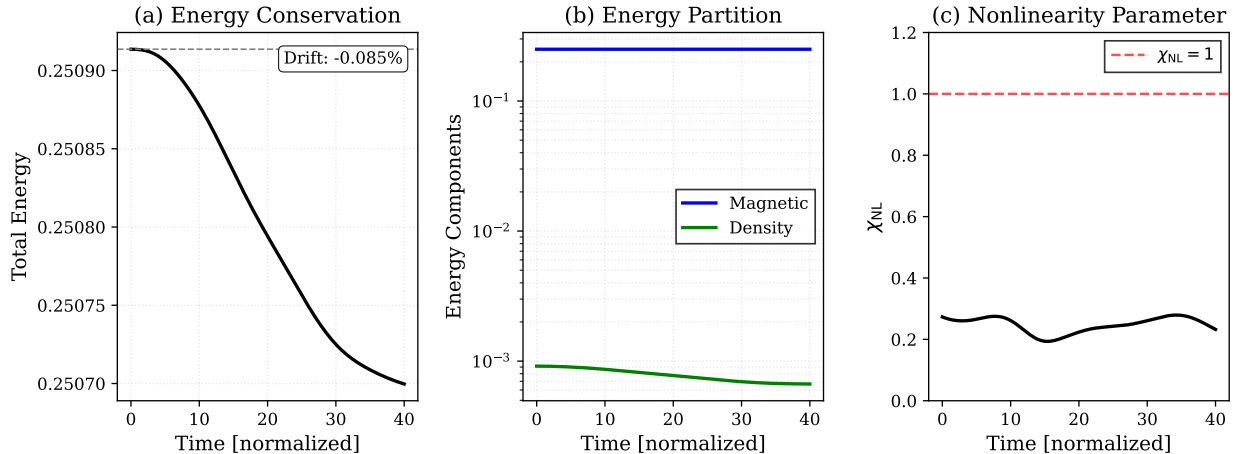


Figure 1: Global diagnostic quantities over the full simulation. (a) Total energy evolution showing a drift of only -0.085% , confirming numerical reliability. (b) Energy partition between magnetic (blue) and density (green) components on a logarithmic scale; the magnetic component dominates by roughly two orders of magnitude throughout. (c) Nonlinearity parameter χ_{NL} as a function of time; values near 0.25, well below the strong-turbulence threshold $\chi_{\text{NL}} = 1$ (red dashed line), confirm sub-Alfvénic operation.

4.2 Temporal Evolution of Magnetic Structures

Figure 2 shows the two-dimensional distribution of the magnetic field intensity $|\delta B_y|^2$ at six times from $t = 0$ to $t = 40$. The initialization at $t = 0$ is spatially irregular without distinct preferred structures. By $t = 8$, elongated filaments of elevated intensity have already emerged from the background, indicating that the broadband turbulence self-organizes on a timescale of order several wave periods, broadly consistent with the nonlinear interaction time $\tau_{\text{nl}} \sim (Q|\delta B_y|^2)^{-1}$ at these amplitudes. By $t = 16$ the filaments are more pronounced, with peak normalized intensities exceeding 1.6 in isolated regions while the surrounding plasma carries much lower intensity.

Through $t = 24$, 32, and 40 the filamentary pattern continues to evolve: structures shift, merge, and re-form. The general character, a spatially intermittent field with localized intensity peaks surrounded by a quiescent background, persists throughout. Such intermittency is characteristic of kinetic-scale turbulence and is consistent with observations of magnetic field structures in the PSBL and magnetosheath (Gershman et al., 2017b; Chen et al., 2019; Sahraoui et al., 2009; Chettri et al., 2026). The perpendicular extents of the structures, of order $10\text{--}20\rho_s$, are comparable to the scales of magnetic holes and enhancements reported by MMS in the plasma sheet boundary layer (Huang et al., 2017; Gershman et al., 2017a).

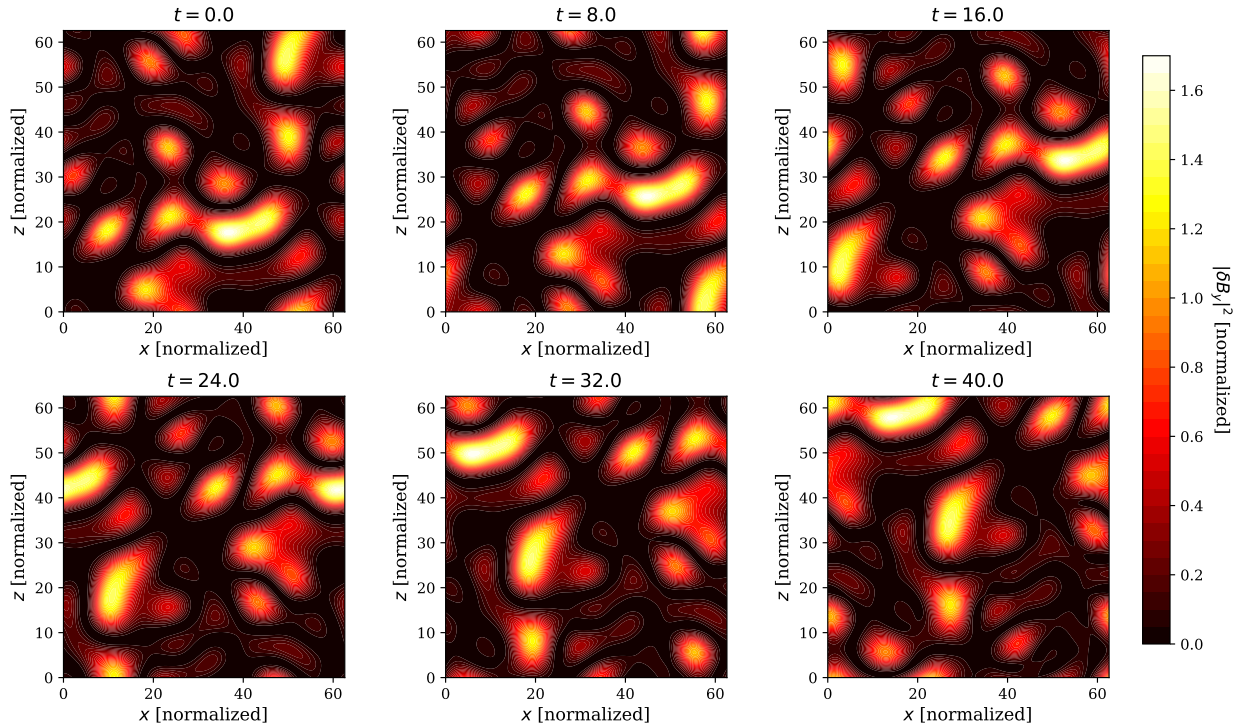


Figure 2: Temporal evolution of the magnetic field intensity $|\delta B_y|^2$ (normalized) at $t = 0, 8, 16, 24, 32, 40$. Elongated, filamentary structures emerge from the initial broadband spectrum and persist throughout. Peak intensities reach ~ 1.6 in isolated regions while the background stays near zero, indicating notable spatial intermittency characteristic of kinetic-scale turbulence.

4.3 Density Cavity Formation and Persistence

Figure 3 shows the corresponding evolution of the normalized density perturbation $\delta n/n_0$ at the same six times. The field displays both positive enhancements (red) and negative depletions (blue), with amplitudes reaching $|\delta n/n_0| \sim 0.3\text{--}0.5$. The spatial pattern closely mirrors, but is not identical to, the magnetic intensity map; in particular, the deepest depletions (dark blue) sit consistently beneath elevated magnetic intensity peaks, the spatial signature of ponderomotive plasma expulsion.

The density structures form on the same timescale as the magnetic ones ($\lesssim 8$ normalized time units) and persist without significant decay to $t = 40$. Prominent depletions co-located with the strongest magnetic filaments are clearly present from $t = 8$ onward and persist through $t = 40$, evolving in shape and depth rather than dispersing. This persistence reflects a sustained quasi-equilibrium between wave pressure and plasma pressure, consistent with the quasi-static limit of equation (7).

The amplitude $|\delta n/n_0| \sim 0.3\text{--}0.5$ is substantially larger than what is typically obtained in single-wave-packet simulations at comparable wave amplitudes (Shukla and Stenflo, 1999). In a broadband initialization, every KAW mode in the spectrum contributes a gradient of wave pressure at its own scale; these contributions add incoherently to produce a sustained, distributed ponderomotive drive that a single wave packet cannot replicate. The resulting density amplitudes approach the 10–30% values reported by MMS in the plasma sheet (Huang et al., 2017; Gershman et al., 2017a).

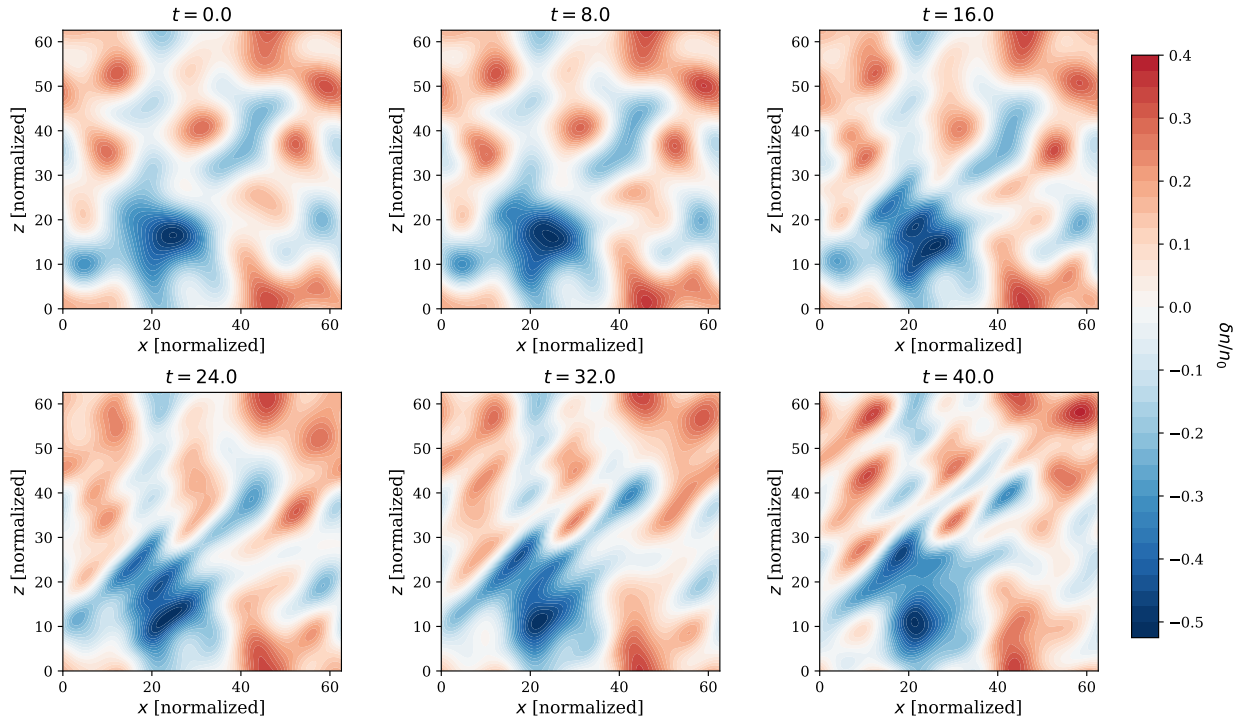


Figure 3: Temporal evolution of the normalized density perturbation $\delta n/n_0$ at $t = 0, 8, 16, 24, 32, 40$. Red regions are density enhancements; blue regions are depletions. Persistent cavities (dark blue, $\delta n/n_0 \lesssim -0.3$) form co-spatially with magnetic intensity peaks, consistent with ponderomotive expulsion. Amplitudes $|\delta n/n_0| \sim 0.3\text{--}0.5$ exceed those found in single-wave-packet runs, reflecting the stronger continuous drive from the broadband initialization.

4.4 Spatial Profiles and Anisotropy

Figure 4 shows one-dimensional cuts through $|\delta B_y|^2$ at three cross-sections in the perpendicular direction x (upper panel, fixed z) and the parallel direction z (lower panel, fixed x). The profiles are irregular rather than periodic or smoothly varying, confirming the turbulent character of the field. Peak intensities vary between cross-sections from near 1.0 to below 0.4, providing a direct, quantitative measure of spatial intermittency. The perpendicular cuts show slightly more localized peaks than the parallel cuts, consistent with the anisotropic nature of KAW fluctuations at $k_\perp \rho_i \sim 1$ and with the MNLS dispersion coefficient P (equation 2) breaking the x - z symmetry at the carrier-wave level (Howes et al., 2008).

The characteristic peak widths of 5–15 normalized units correspond to physical scales within the 5–20 d_i range of ion-scale magnetic structures observed by multiple MMS studies in the plasma sheet and its boundary layer (Huang et al., 2017; Gershman et al., 2017a).

4.5 Magnetic Energy Spectra

Figure 5 shows time-averaged magnetic energy spectra in the perpendicular (k_\perp) and parallel (k_\parallel) directions, averaged over the final two-thirds of the run to capture quasi-steady conditions. The Kolmogorov–Goldreich–Sridhar inertial-range slopes $k_\perp^{-5/3}$ and $k_\parallel^{-7/3}$ are shown as dashed reference lines anchored in the injection region; their purpose is to make visible the immediate departure of the simulated spectrum from the theoretical inertial-range

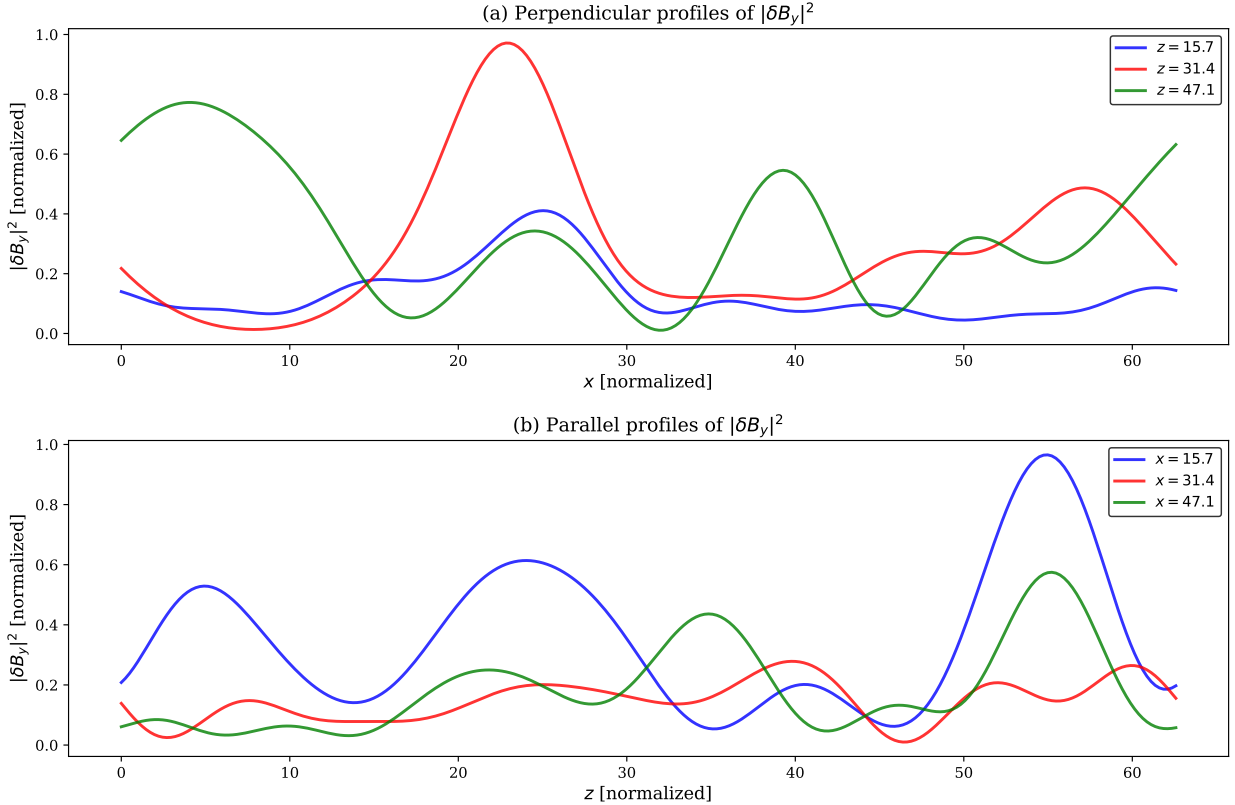


Figure 4: One-dimensional profiles of $|\delta B_y|^2$ (normalized). (a) Perpendicular cuts at $z = 15.7, 31.4,$ and 47.1 . (b) Parallel cuts at $x = 15.7, 31.4,$ and 47.1 . Peak intensities reach ~ 1.0 in both directions with structure widths of 5–15 normalized units, consistent with ion-scale magnetic structures observed by MMS in the plasma sheet boundary layer.

prediction, not to assert that such a range is present.

The perpendicular spectrum is approximately flat for $k_\perp < 0.3$, where most energy resides, and steepens sharply beyond $k_\perp \sim 0.3$ – 0.5 , dropping by many orders of magnitude before reaching the dissipation floor near $k_\perp \sim 2$. A brief spectral re-enhancement near $k_\perp \approx 0.5$ may reflect a local energy pile-up at the KAW dispersion scale $k_\perp \rho_s \sim 1$; similar pile-ups have been observed in solar wind spectra near the ion gyroscale (Bale et al., 2005; Sahaoui et al., 2009; Chen et al., 2013). No extended power-law inertial range is present between injection and dissipation.

The parallel spectrum shows a broadly similar shape: energy concentrated at low k_\parallel , a broad transition region, and a steep drop at $k_\parallel \gtrsim 0.5$. It falls somewhat less steeply than the perpendicular spectrum at intermediate scales, consistent with weaker damping of field-aligned fluctuations in the absence of the full anisotropic kinetic damping tensor (Schekochihin et al., 2009). The absence of an extended inertial range is physically meaningful and is discussed further in Section 5.2.

5 Discussion

5.1 Ponderomotive Structuring in Broadband Turbulence

The results demonstrate that ponderomotive density cavity formation is not confined to the idealized case of a single wave packet propagating through a quiescent plasma. In the

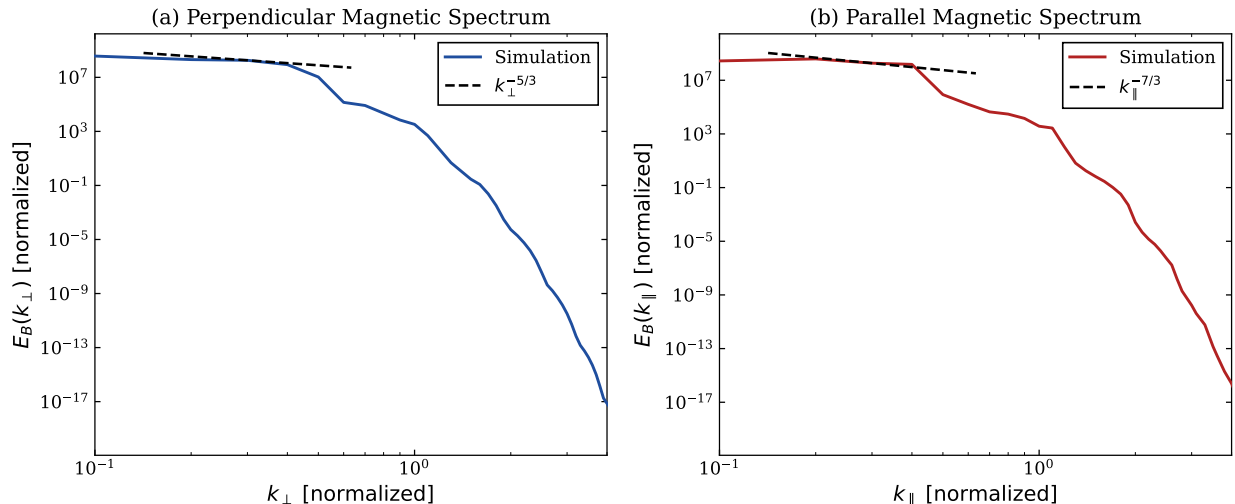


Figure 5: Time-averaged magnetic energy spectra. (a) Perpendicular spectrum $E_B(k_\perp)$: energy is concentrated at large injection scales ($k_\perp \lesssim 0.3$) and falls steeply without forming an extended power-law range before reaching the dissipation floor near $k_\perp \sim 2$. (b) Parallel spectrum $E_B(k_\parallel)$: qualitatively similar, with a somewhat less steep transition consistent with weaker damping of field-aligned fluctuations. In both panels the dashed line shows the theoretical inertial-range slope ($k^{-5/3}$ perpendicular; $k^{-7/3}$ parallel) anchored at the injection scale as a reference; the immediate and sustained departure of the simulated spectrum from this slope confirms the absence of an inertial range, consistent with the moderate Reynolds number of PSBL turbulence ($\text{Re} \sim 7\text{--}110$ from spacecraft observations; see Section 5.2).

broadband turbulent simulations presented here, multiple coexisting KAW modes collectively drive a spatially distributed pattern of density depletions and enhancements that emerges spontaneously and persists throughout the run. Every mode in the broadband initialization contributes a gradient of wave pressure at its own scale; these contributions add incoherently, producing a continuous ponderomotive drive spread across the domain that a single wave packet cannot replicate. This accounts for the order-of-magnitude increase in density amplitude relative to single-packet runs at comparable wave amplitudes (Shukla and Stenflo, 1999), and brings the simulated amplitudes into much closer agreement with the 10–30% density fluctuations reported by MMS in the plasma sheet (Huang et al., 2017; Gershman et al., 2017a; Chettri et al., 2026).

5.2 Reynolds Number Constraints and Spectral Character

The absence of an extended power-law inertial range in the energy spectra (Figure 5) warrants careful interpretation. The magnetic Reynolds number achievable in a kinetic-scale simulation scales as $\text{Rm} \sim A \times N_{\text{grid}}^{4/3}$ (Mininni et al., 2004), placing our 256×256 run in the range $\text{Re} \sim 250\text{--}370$. This is above the critical threshold for turbulent cascade development in collisionless plasmas ($\text{Rm}_{\text{crit}} \approx 107\text{--}124$; St-Onge et al. 2020) but far below the solar wind value of $\text{Re} \sim 10^5$. Importantly, spacecraft observations in Earth’s plasma sheet yield $\text{Re} \sim 7\text{--}110$ (Weygand et al., 2007), which directly overlaps with our simulation range. The rapid injection-to-dissipation transition seen in our spectra is therefore not a numerical deficiency but an accurate representation of the physical regime in which PSBL turbulence operates.

In the solar wind, where $\text{Re} \sim 10^5\text{--}10^6$, the Kolmogorov inertial range spans several

decades and a $k^{-5/3}$ spectrum is unambiguous (Bale et al., 2005; Sahraoui et al., 2009). In the magnetotail, no such separation of scales exists: the cascade in wavenumber space is compressed to at most one or two decades, and any spectral index extracted from a short power-law segment is strongly sensitive to the fitting range. Our simulations reproduce this compression faithfully, and they caution against over-interpreting spectral slopes derived from short PSBL data intervals. The same constraint applies to the reference slopes shown in Figure 5: the predictions of Goldreich and Sridhar (1995) and Boldyrev and Perez (2012) for critically balanced Alfvénic turbulence assume $\text{Re} \gg 1$ and are not directly applicable to the low-Reynolds-number PSBL environment.

5.3 Sub-Alfvénic Operation and Astrophysical Relevance

The nonlinearity parameter $\chi_{\text{NL}} \approx 0.25$ throughout places the system in the sub-Alfvénic (or weak turbulence) regime, where wave periods are shorter than the nonlinear interaction time and energy transfer proceeds primarily through resonant three-wave interactions (Galtier et al., 2000). Ponderomotive density structures form efficiently here because the wave coherence time is long enough to sustain a quasi-static pressure gradient, in agreement with the analytical predictions of Shukla and Stenflo (1999).

The broader implications extend to several astrophysical environments. In the solar corona and solar wind, KAW ponderomotive structuring is a candidate mechanism for density striations that produce enhanced radio scintillation (Cranmer and van Ballegooijen, 2012; Matthaeus and Velli, 2011). In the inner heliosphere, coupled KAW and ion-acoustic wave dynamics have been identified in Parker Solar Probe observations (Chettri et al., 2024), lending further support to the ubiquity of ponderomotive coupling across heliospheric environments. In the interstellar medium, kinetic-scale Alfvénic turbulence governs pulsar scattering and cosmic-ray transport through pitch-angle scattering (Lazarian and Berezhnaya, 2006; Yan and Lazarian, 2004). In galaxy clusters, kinetic instabilities akin to KAW ponderomotive coupling are invoked to explain density fluctuations below the Coulomb mean free path in the hot intracluster medium (Brunetti and Lazarian, 2007; Schekochihin et al., 2009). The ICM parameters ($\beta \sim 50\text{--}100$; length scales of kiloparsecs) differ enormously from the PSBL studied here, but the governing kinetic-scale wave equations share the same mathematical structure. The central conclusion of the present work therefore applies to these environments by appropriate parameter scaling (Verscharen et al., 2019; Schekochihin et al., 2009).

5.4 Limitations

Several limitations of the present model motivate follow-on work. The simulations are two-dimensional, so three-dimensional effects such as field-aligned focusing of wave energy and anisotropic cascade development (Goldreich and Sridhar, 1995) are absent. The parallel-propagation approximation adopted for the density equation (6) neglects cross-field acoustic transport; at higher β , where C_s approaches v_A , the full Laplacian ∇^2 should be retained. The MNLS framework (equation 1) incorporates Landau damping through a scalar coefficient Γ ; it does not resolve the full anisotropic, wave-vector-dependent kinetic damping tensor captured by gyrokinetic descriptions (Schekochihin et al., 2009; Howes et al., 2008). Ion temperature is held constant, suppressing the pressure anisotropy feedback and mirror-mode-like saturation that could develop in a fully kinetic treatment at higher β . Wave-particle resonances, particularly the electron Landau channel identified by Chen et al. (2019) and the ion heating inferred from MMS energy-flux measurements (Gershman et al.,

2017b), are not self-consistently resolved by the fluid-envelope approach.

6 Summary and Conclusions

We have presented two-dimensional pseudospectral simulations of the MNLS–magnetosonic system under plasma-sheet-boundary-layer conditions ($\beta \sim 0.1$ – 0.3), initialized with a broadband turbulent spectrum spanning many simultaneously active wave modes. The governing equations follow the modified nonlinear Schrödinger framework of [Chettri et al. \(2025\)](#), and the key questions concern how turbulent multi-mode driving, rather than a single wave packet, shapes density structuring, spectral character, and Reynolds-number physics under low- β PSBL conditions. The main findings are as follows.

1. Total energy is conserved to within 0.085% over the full integration to $t = 40$ normalized units, with hyperviscous dissipation confined to grid scales, confirming the numerical reliability of the RK4 pseudospectral solver.
2. The simulation operates in the sub-Alfvénic turbulent regime throughout ($\chi_{\text{NL}} \approx 0.25$, well below the strong-turbulence threshold), placing the results in the range relevant to quieter PSBL intervals and to sub-Alfvénic turbulence in a variety of astrophysical environments.
3. Spatially intermittent, filamentary magnetic structures emerge from the broadband initialization within a few wave periods and persist throughout the run. Their perpendicular scales, ~ 10 – $20 \rho_s$, are consistent with ion-scale magnetic structures observed by MMS in the plasma sheet boundary layer ([Huang et al., 2017](#); [Gershman et al., 2017a](#); [Chettri et al., 2026](#)).
4. Persistent density cavities with amplitudes $|\delta n/n_0| \sim 0.3$ – 0.5 form co-spatially with magnetic intensity peaks, confirming ponderomotive expulsion of plasma from wave-intense regions. These amplitudes are substantially larger than those produced by single-wave-packet simulations at comparable wave amplitudes, demonstrating that broadband turbulent driving enhances ponderomotive density structuring.
5. The magnetic energy spectra exhibit a rapid injection-to-dissipation transition without an extended inertial range, consistent with the moderate magnetic Reynolds number of both the simulation ($\text{Re} \sim 250$ – 370) and the actual PSBL plasma ($\text{Re} \sim 7$ – 110 from spacecraft observations). The absence of a power-law inertial range is an intrinsic feature of this turbulent regime, not a numerical artefact.

These results show that ponderomotive density structuring by KAW turbulence is not restricted to the idealized single-wave-packet limit but operates equally well under broadband turbulent driving. The spectral character of kinetic-scale turbulence in low-Reynolds-number environments such as the PSBL is qualitatively distinct from that of the solar wind, and spectral slopes extracted from short data intervals in this regime should be interpreted with care. The MNLS pseudospectral approach used here is fast enough to permit systematic parameter surveys of how density structuring depends on β , wave amplitude, and injection scale.

Future work should extend the simulations to three dimensions to capture field-aligned focusing, incorporate kinetic physics through hybrid or gyrokinetic approaches to resolve Landau damping more completely, and carry out direct event-by-event comparisons with MMS burst-mode intervals in which KAW activity and density structuring are simultaneously resolved.

Acknowledgements

Authors MKC, VS, and BS acknowledge the University Grants Commission (UGC), India, for support through the Non-NET Fellowship programme. One of the authors RM acknowledges support from IUCAA Pune through visiting associate program.

References

- Bale, S. D., Kellogg, P. J., Mozer, F. S., Horbury, T. S., and Reme, H. (2005). Measurement of the electric fluctuation spectrum of magnetohydrodynamic turbulence. *Physical Review Letters*, 94:215002.
- Boldyrev, S. and Perez, J. C. (2012). Spectrum of kinetic-Alfvén turbulence. *The Astrophysical Journal Letters*, 758:L44.
- Brunetti, G. and Lazarian, A. (2007). Compressible turbulence in galaxy clusters: physics and stochastic particle re-acceleration. *Monthly Notices of the Royal Astronomical Society*, 378:245–275.
- Chaston, C. C., Bonnell, J. W., Carlson, C. W., McFadden, J. P., Mozer, F., Ergun, R. E., and Strangeway, R. J. (2008). Kinetic effects in the acceleration of auroral electrons in small-scale Alfvén waves: a FAST case study. *Geophysical Research Letters*, 35:L02105.
- Chen, C. H. K., Boldyrev, S., Xia, Q., and Perez, J. C. (2013). Nature of sub-proton scale turbulence in the solar wind. *Physical Review Letters*, 110:225002.
- Chen, C. H. K., Klein, K. G., and Howes, G. G. (2019). Evidence for electron Landau damping in space plasma turbulence. *Nature Communications*, 10:740.
- Chettri, M. K., Shrivastav, V., Mukherjee, R., Gaur, N., Sharma, R., and Singh, H. D. (2024). Nonlinear coupling of kinetic Alfvén waves and ion acoustic waves in the inner heliosphere. *Research in Astronomy and Astrophysics*, 24(10):105009.
- Chettri, M. K., Singh, H. D., and Mukherjee, R. (2026). Mms observations of kinetic Alfvén wave turbulence and steep kinetic-range spectra in the outer plasma sheet boundary layer. *arXiv preprint arXiv:2603.07969*.
- Chettri, M. K., Singh, H. D., Shrivastav, V., Singh, B., and Mukherjee, R. (2025). Damped kinetic Alfvén waves in earth’s magnetosheath: Numerical simulations and mms observations. *arXiv preprint arXiv:2512.09828*.
- Cranmer, S. R. and van Ballegoijen, A. A. (2012). Proton, electron, and ion heating in the fast solar wind from nonlinear coupling between Alfvénic and fast-mode turbulence. *The Astrophysical Journal*, 754:92.
- Denton, R. E. et al. (2010). Multiple harmonic ULF waves in the plasma sheet boundary layer: instability analysis. *Journal of Geophysical Research*, 115:A12224.
- Du, A. M. et al. (2011). Fast tailward flows in the plasma sheet boundary layer during a substorm on 9 March 2008: THEMIS observations. *Journal of Geophysical Research*, 116:A03216.

- Galtier, S., Nazarenko, S. V., Newell, A. C., and Pouquet, A. (2000). A weak turbulence theory for incompressible magnetohydrodynamics. *Journal of Plasma Physics*, 63:447–488.
- Gershman, D. J. et al. (2017a). Magnetic holes in a kinetic turbulent plasma. *Journal of Geophysical Research: Space Physics*, 122:11108–11120.
- Gershman, D. J. et al. (2017b). Wave-particle energy exchange directly observed in a kinetic Alfvén-branch wave. *Nature Communications*, 8:14719.
- Goldreich, P. and Sridhar, S. (1995). Toward a theory of interstellar turbulence. II. strong Alfvénic turbulence. *The Astrophysical Journal*, 438:763–775.
- Hasegawa, A. and Chen, L. (1976). Parametric decay of “kinetic Alfvén wave” and its application to plasma heating. *Physical Review Letters*, 36:1362–1365.
- Howes, G. G., Cowley, S. C., Dorland, W., Hammett, G. W., Quataert, E., and Schekochihin, A. A. (2008). A model of turbulence in magnetized plasmas: implications for the dissipation range in the solar wind. *Journal of Geophysical Research: Space Physics*, 113:A05103.
- Huang, S. Y. et al. (2017). MMS observations of ion-scale magnetic holes in the plasma sheet. *Geophysical Research Letters*, 44:7131–7139.
- Lazarian, A. and Beresnyak, A. (2006). Cosmic ray scattering in compressible turbulence. *Monthly Notices of the Royal Astronomical Society*, 373:1195–1202.
- Leamon, R. J., Smith, C. W., Ness, N. F., and Wong, H. K. (1999). Dissipation range dynamics: kinetic Alfvén waves and the importance of β_e . *Journal of Geophysical Research*, 104:22331–22344.
- Matthaeus, W. H. and Velli, M. (2011). Who needs turbulence? A review of turbulence effects in the heliosphere and on the fundamental process of reconnection. *Space Science Reviews*, 160:145–168.
- Mininni, P. D., Gómez, D. O., and Mahajan, S. M. (2004). Dynamo action in magnetohydrodynamics and Hall-magnetohydrodynamics. *The Astrophysical Journal*, 587:472–481.
- Roberts, O. W. et al. (2018). Observation of an MHD Alfvén vortex in the slow solar wind. *Journal of Geophysical Research: Space Physics*, 123:6998–7009.
- Sahraoui, F., Goldstein, M. L., Robert, P., and Khotyaintsev, Y. V. (2009). Evidence of a cascade and dissipation of solar-wind turbulence at the electron gyroscale. *Physical Review Letters*, 102:231102.
- Schekochihin, A. A. et al. (2009). Astrophysical gyrokinetics: kinetic and fluid turbulent cascades in magnetized weakly collisional plasmas. *The Astrophysical Journal Supplement Series*, 182:310–377.
- Shrivastava, G., Shrivastava, J., and Ahirwar, G. (2015). Kinetic Alfvén wave in the presence of kappa distribution function in the plasma sheet boundary layer. In *AIP Conference Proceedings*, volume 1670, page 030031.

- Shukla, P. K. and Stenflo, L. (1999). Nonlinear propagation of kinetic Alfvén waves. *Physics of Plasmas*, 6:4120–4124.
- St-Onge, D. A., Kunz, M. W., Squire, J., and Schekochihin, A. A. (2020). Fluctuation dynamo in a collisionless, weakly magnetized plasma. *Journal of Plasma Physics*, 86:905860503.
- Stawarz, J. E. et al. (2017). Magnetospheric Multiscale analysis of intense field-aligned Poynting flux near the Earth’s plasma sheet boundary. *Geophysical Research Letters*, 44:7106–7113.
- Terradas, J., Soler, R., Oliver, R., and Ballester, J. L. (2022). Parametric decay of standing Alfvén waves in a coronal loop. *Astronomy & Astrophysics*, 660:A136.
- Verscharen, D. et al. (2024). Parametric decay instability of circularly polarised Alfvén waves with a spectrum of wavevectors: 3D hybrid simulations. arXiv preprint arXiv:2403.08179.
- Verscharen, D., Klein, K. G., and Maruca, B. A. (2019). The multi-scale nature of the solar wind. *Living Reviews in Solar Physics*, 16:5.
- Weygand, J. M. et al. (2007). Plasma sheet turbulence observed by Cluster II. *Journal of Geophysical Research: Space Physics*, 112:A10201.
- Wygant, J. R. et al. (2002). Evidence for kinetic Alfvén waves and parallel electron energization at 4–6 r_e altitudes in the plasma sheet boundary layer. *Journal of Geophysical Research: Space Physics*, 107:1201.
- Yan, H. and Lazarian, A. (2004). Cosmic-ray scattering and streaming in compressible magnetohydrodynamic turbulence. *The Astrophysical Journal*, 614:757–769.
- Zhou, X.-Z. et al. (2012). Emergence of the active magnetotail plasma sheet boundary from transient, localized ion acceleration. *Journal of Geophysical Research*, 117:A10216.